American Mineralogist, Volume 94, pages 801–815, 2009

Two types of metamorphic monazite with contrasting La/Nd, Th, and Y signatures in an ultrahigh-pressure metapelite from the Pohorje Mountains, Slovenia: Indications for pressure-dependent REE exchange between apatite and monazite?

Erwin Krenn,[1,*] Marian Janák,[2] Fritz Finger,[1] Igor Broska,[2] and Patrik Konečný[3]

[1]Department of Materials Engineering and Physics, University of Salzburg, Hellbrunnerstrasse 34, 5020 Salzburg, Austria
[2]Geological Institute, Slovak Academy of Sciences, Dúbravská cesta 9, 840 05 Bratislava, Slovak Republic
[3]Dionýz Štúr Institute of Geology, Mlynská dolina 1, 817 04 Bratislava, Slovak Republic

Abstract

Two monazite generations (M1; M2) were distinguished in a kyanite-garnet gneiss from the UHP terrain of the Pohorje Mountains, Slovenia. *P-T* estimates reveal a peak event at 760 °C/2.6 GPa and isothermal decompression down to 700 °C/0.6 GPa.

M1 type provides a Th-U-Pb mean date of 100 ± 6 Ma, ThO_2 contents between 3–7 wt%, Y_2O_3 values <0.3 wt%, and La/Nd ratios (1.2–1.4) that are clearly higher than for the whole-rock La/Nd (1.1). The absence of Y zoning in M1 and the lack of monazite inclusions in garnet indicate that M1 formed after the main stage of garnet growth (>1.2 MPa), probably close to the *P-T* peak.

M2 type is slightly younger than M1 (74 ± 16 Ma), and has a lower La/Nd (0.3–0.9), lower ThO_2 (0.1–5 wt%), and higher Y_2O_3 (up to 3.2 wt%). Most M2 monazites occur as tiny needles within apatite (subtype M2-a) or along apatite margins (M2-b). Parasitic growth of M2-a and -b from apatite is supported by its low ThO_2 (<1 wt%) and La/Nd (<0.5). Isolated matrix grains (M2-c) and overgrowths around M1 (M2-d) have slightly higher La/Nd (0.5–0.9) and higher ThO_2 (5 wt%) and were supplied from an apatite and M1 source. Elevated yttrium suggests that M2 formed during decompression, when garnet was consumed and Y was released.

These observations imply that at UHP conditions MREE-rich apatite coexisted with low-MREE M1 monazite and reacted during decompression to Ca-F-apatite plus MREE-rich M2 monazite. This provides strong arguments that REE-partitioning between apatite and monazite is pressure-dependent.

Keywords: Monazite, apatite, REE distribution, ultra-high pressure, Pohorje Mountains

Introduction

Since growth ages of monazite can be precisely determined by means of Th-U-Pb geochronology, there is much interest in its behavior during metamorphic processes. The formation of metamorphic monazite, especially under lower amphibolite-facies conditions, often involves breakdown of allanite as the LREE-bearing source (Bingen et al. 1996; Finger et al. 1998; Spear and Pyle 2002; Wing et al. 2003; Cho et al. 2006; Yang et al. 2006; Janots et al. 2006, 2008; Krenn and Finger 2007; Tomkins and Pattison 2007; Corrie and Kohn 2008). However, metamorphic monazite might also form through direct replacement of an older monazite. Although this process is especially common at higher metamorphic conditions (upper-amphibolite and granulite facies), where the mechanism of monazite dissolution-reprecipitation is important (McFarlane et al. 2006; Finger and Krenn 2007), it might also operate at lower-grade conditions (e.g., Rasmussen et al. 2007; Janots et al. 2008). Comparably rare are reports of monazite-forming processes involving REE-bearing phases such as rhabdophane or florencite (e.g., Sawka et al. 1986; Nagy et al. 2002), REE oxides (Kingsbury et al. 1993), REE-carbonates, or major rock-forming minerals (Kohn and Malloy 2004).

There are also reports that under certain circumstances metamorphic monazite can form by reaction from LREE-bearing apatite (Pan et al. 1993; Harlov and Förster 2002; Harlov et al. 2005; Ziemann et al. 2005). Arguments for monazite formation at the expense of LREE-enriched apatite are mainly textural and are based upon the occurrence of secondary monazite needles within apatite (Liou et al. 1998; Zhang and Liou 1999; Harlov and Förster 2002), secondary monazite seams around apatite, or parasitic monazite rim grains nucleating at apatite grain boundaries (Finger and Krenn 2007).

Harlov and Förster (2002) and Harlov et al. (2005) have confirmed, by means of hydrothermal experiments, that natural apatite, if LREE-rich, can metasomatically react to form LREE-poor apatite plus monazite. Back-scattered electron images (BSE) of the run products document a process of replacement of the original apatite, preferentially at its margin and along cracks, which is coupled with the nucleation and growth of small monazite crystals in these zones. The reaction in this case was clearly driven by a dissolution-reprecipitation process. Based on their experiments, Harlov et al. (2005) argued that monazite formation from apatite is mostly metasomatic in nature as well and requires the presence of suitable fluids. However, it is debatable whether at higher temperatures the process is driven simply by solid-state diffusion (Tacker and Stormer 1989; Finger and Krenn 2007), which is known to be fast in apatite (Cherniak and

* E-mail: erwin.krenn@sbg.ac.at

Ryerson 1993; Cherniak et al. 2004).

Regardless of which mechanism triggers monazite formation from apatite, this process will be significant only when sufficiently LREE-enriched apatite is available. Fleet and Pan (1997) demonstrated that apatite can accommodate several wt% REEs. However, accessory apatite in metamorphic rocks rarely has a REE content of greater than 1 wt%. Bingen et al. (1996) suggested that the contents of lanthanides and actinides in metamorphic apatite increase with metamorphic grade. Later, it was proposed by Spear and Pyle (2002) and Finger and Krenn (2007) that, particularly under high-pressure conditions, apatite may become an important REE carrier, and that REE-rich high-pressure apatite may thus serve as a fertile source for retrograde monazite growth on the decompression path.

In this study, we discuss a kyanite-garnet gneiss from the Pohorje Mountains, Slovenia, that underwent ultrahigh-pressure (UHP) metamorphism. This rock provides a "natural laboratory" for studying monazite-forming processes, monazite-apatite phase relations, and REE exchange between these phases in a high-*P*, high-*T* system.

Geological background

The Pohorje Mountains in Slovenia represent a famous exposure of Cretaceous ultrahigh-pressure rocks in the Alps (Janák et al. 2004, 2006). Metamorphic processes related to the Cretaceous, so-called "Eoalpine," events have been recognized throughout the Alps but mainly in the Austroalpine units (Thöni and Jagoutz 1992; Hoinkes et al. 1999; Schmid et al. 2004; Schuster et al. 2004). In the Eastern Alps, the Cretaceous metamorphism reached ultrahigh-pressure facies only in the southeasternmost sector, in the Pohorje Mountains (Fig. 1), which represents part of the Lower Central Austroalpine unit (Janák et al. 2004, 2006; Oberhänsli et al. 2004). Janák et al. (2004) obtained *P-T* conditions of 3.0–3.1 GPa and 760–825 °C for kyanite eclogites from the Pohorje Mountains, which correspond to UHP metamorphism in the stability field of coesite. Garnet peridotites yield UHP conditions as high as ca. 4.0 GPa at 900 °C (Janák et al. 2006). Other Pohorje eclogites, which were studied by Sassi et al. (2004) and Miller et al. (2005), equilibrated at lower-pressure conditions.

The Eoalpine high- to ultrahigh-pressure metamorphism in the Eastern Alps is related to collision between the Austroalpine Unit and another continental fragment or an island arc, following the closure of the Meliata-Hallstatt Ocean (Thöni and Jagoutz 1992; Froitzheim et al. 1996; Stampfli et al. 1998). Subduction was intracontinental (Janák et al. 2004) with the northwestern (i.e., Lower Central) parts of the Austroalpine Unit subducted under the southeastern parts (Upper Central Austroalpine).

The Pohorje Mountains comprise three lithostratigraphic units forming a nappe stack: (1) a lowest nappe of medium- to high-grade metamorphic rocks; (2) a middle nappe of low-grade Palaeozoic metasediments with remnants of their Permo-Mesozoic cover; and (3) an uppermost nappe built up of unmetamorphosed Permo-Triassic sediments. This nappe stack is overlain by Early Miocene sediments, which belong to the syn-rift Pannonian Basin (Fodor et al. 2003). The structure of the Pohorje massif is that of a large antiform with an ESE-WNW-striking axis and cored by a ca. 18–19 Ma granodiorite to tonalite pluton (Altherr et al. 1995; Fodor et al. 2008; Trajanova et al. 2008).

The lowest nappe, which represents the Lower Central Austroalpine unit (Janák et al. 2004), consists predominantly of mica schists, gneisses, and amphibolites with marble and quartzite lenses. In the southeastern part, there are numerous eclogites and large bodies of ultramafic rocks (serpentinites and garnet peridotites). All of these rocks are strongly foliated and underwent high- to ultrahigh-pressure metamorphism related to Eoalpine subduction in Late Cretaceous time, as documented by geochronological data (Thöni 2002; Miller et al. 2005; Cornell et al. 2007).

Petrography and mineral compositions

The monazite-bearing kyanite-garnet gneiss investigated in this study occurs in the southern part of the Pohorje Mountains near the village of Jurišna Vas (Fig. 1b). The gneiss hosts several lenses of eclogites exhibiting shear fabrics related to deformation during exhumation. The major mineral phases of the gneiss are quartz (~25 modal %), biotite (~15%), white mica (35–40%), garnet (~10%), and plagioclase (5–10%), with minor kyanite, potassium feldspar, staurolite, rutile, and apatite. Compositions of the major mineral phases (Table 1) were determined using a CAMECA SX-100 electron microprobe at the Dionýz Štúr Institute of Geology in Bratislava. Analytical conditions were 15 kV accelerating voltage and 20 nA beam current, with a peak counting time of 20 s and a beam diameter of 2–10 μm. Raw counts were corrected using a PAP routine.

Analytical methods

Garnet. Garnet forms porphyroblasts up to 0.5 cm in diameter, which are mostly subhedral and slightly elongated parallel to the foliation (Fig. 2a). Some exhibit resorption and fracturing. Microprobe traverses show that the garnet grains have homogeneous cores with higher pyrope (25–27 mol%) and grossular (9–10 mol%) contents, compared to the rims (10–19 mol% pyrope and 6–9 mol% grossular). The decrease in Mg and Ca is balanced by an increase in Fe and Mn (Table 1). Inclusions of kyanite, quartz, Mg-rich biotite [X_{Mg} = Mg/(Mg+Fe) = 0.76–0.79], staurolite, rutile, zircon, apatite, and a carbon phase identified as graphite by Raman spectroscopy can be seen in the garnet cores. Many garnets are affected by retrogression, mostly at the rims but also along microfractures that penetrate the garnet interiors. Several staurolite-biotite-quartz aggregates occur in the retrograded garnet domains. Here, staurolite and biotite are less magnesian then those enclosed in non-retrogressed garnet. Fe-rich biotite (X_{Mg} = 0.42–0.69) and plagioclase occur along the retrogressed rims of garnet.

Phengite. Phengite with up to 3.3 Si apfu (Table 1) is rarely preserved and is mostly decomposed to symplectites of biotite, plagioclase, K-feldspar, and quartz. Kyanite is transformed partly to sillimanite and muscovite, and late staurolite has been observed along the rims of such kyanite. Rutile appears as two varieties: (1) thin, oriented needles of bluish color in garnet (Figs. 2a and 2b) and (2) coarser, randomly oriented red-brownish grains in the matrix. Oriented rutile needles in garnet are considered as important UHP indicators, having unmixed from the formerly Ti-rich garnet during decompression (Ringwood and Lovering 1970; Thompson 1975; Kai et al. 2000; Mposkos and

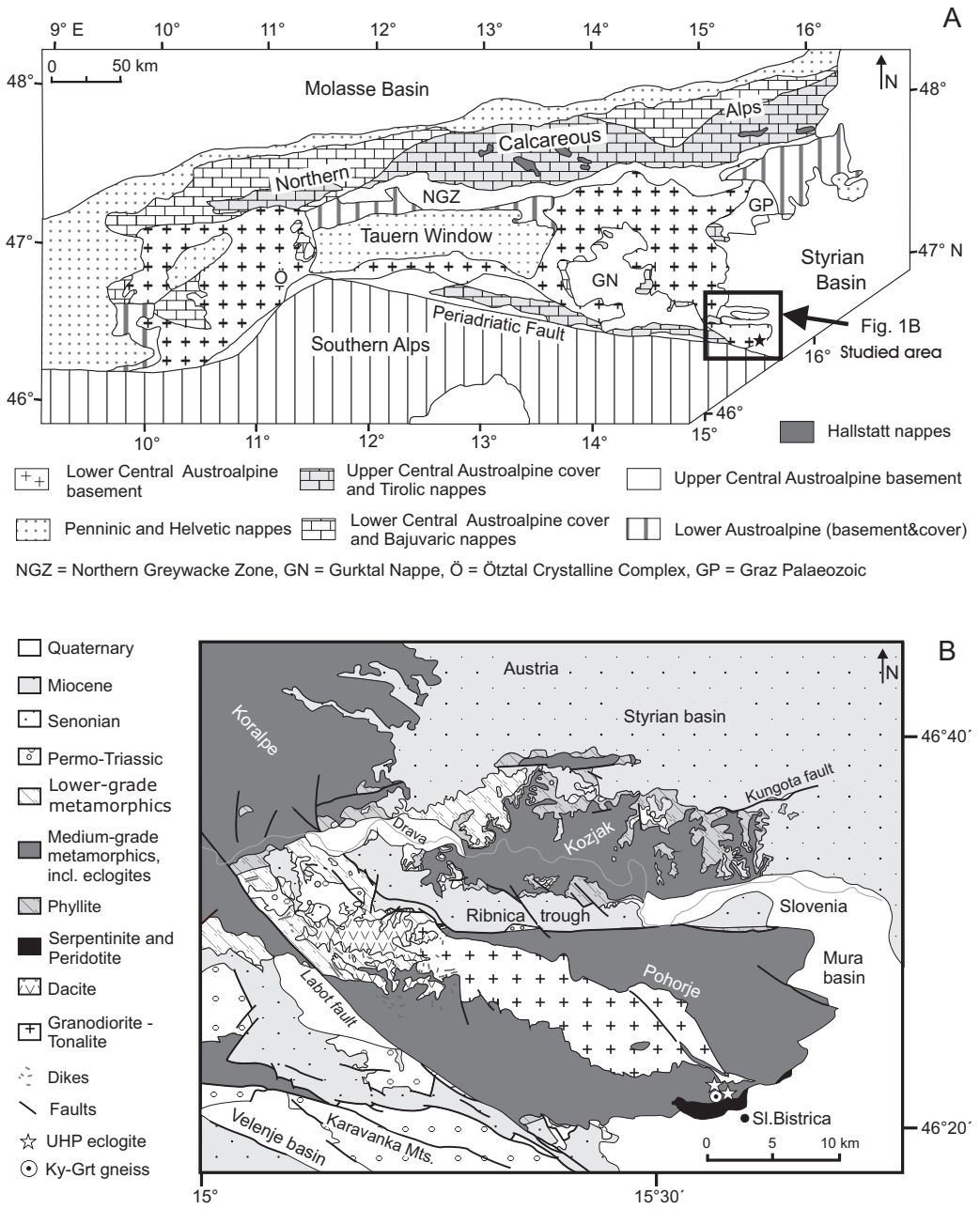

FIGURE 1. Simplified geologic map of the Pohorje Mountains, Slovenia, and their position within the tectonic framework of the Eastern Alps. Modified after Mioč and Žnidarčič (1997), Neubauer and Höck (2000), and Schmid et al. (2004).

Kostopoulos 2001; Zhang and Liou 2003). However, Hwang et al. (2007) have recently questioned this model and proposed that the rutile needles can form by cleaving and healing of garnet coupled with rutile deposition. The major Ti-phase within the secondary matrix is ilmenite. Ilmenite occurs as elongated grains, up to a few hundreds of micrometers in length, preferentially within and along cleavage planes of Fe-rich biotite.

Apatite. Apatite is a widespread accessory mineral in the gneiss. It is variable in size, ranging from a few tens of micrometers up to ca. 0.5 mm. Apatite inclusions in garnet are sometimes euhedral, whereas apatite in the matrix often displays irregular, embayed grain boundaries. In thin section, it is observed that the apatite occasionally contains needle-like inclusions with high relief (Fig. 2c), which resemble the fine rutile needles in the garnet. However, these needles in the apatite are actually monazite, as determined by electron microprobe. Larger grains of monazite and grains of xenotime and zircon were also observed in thin section.

Whole-rock geochemistry

The whole-rock composition of sample P06, which forms the basis of this study, was determined by standard XRF methods,

TABLE 1. Compositions of major mineral phases in the kyanite-garnet gneiss

Sample mineral	JV4 Grt core	JV4 Grt rim	JV4 Phg	JV4 Bt in Grt	JV4 Bt matrix	JV4 Pl rim
SiO_2	38.49	37.68	50.74	39.14	36.21	62.73
TiO_2	0.04	<0.01	0.23	1.19	2.45	<0.01
Al_2O_3	21.66	21.2	30.48	18.25	19.31	23.93
Cr_2O_3	0.04	0.01	0.01	0.03	0.06	<0.01
FeO	30.1	34	3.29	10.5	20.14	<0.01
MnO	0.52	4.02	0.00	0.05	0.16	<0.01
MgO	6.98	2.67	1.67	17.93	8.04	<0.01
CaO	3.4	1.7	0.25	0.08	0.07	5.19
Na_2O	0.01	<0.01	0.10	0.9	0.26	8.53
K_2O	<0.01	<0.01	8.93	7.33	8.58	0.19
Total	101.24	101.28	95.7	95.4	95.28	100.57
Si (apfu)	2.967	3.004	3.333	2.792	2.745	2.761
Ti	0.002	–	0.011	0.064	0.14	–
Al	1.969	1.993	2.361	1.535	1.726	1.242
Cr	0.002	0.001	0.001	0.002	0.004	–
Fe^{3+}	0.091	–	0.053	0.094	–	–
Fe^{2+}	1.85	2.267	0.127	0.532	1.277	–
Mn	0.034	0.271	–	0.003	0.01	–
Mg	0.802	0.317	0.163	1.906	0.908	–
Ca	0.281	0.145	0.018	0.006	0.006	0.245
Na	0.001	–	0.013	0.124	0.038	0.728
K	–	–	0.749	0.668	0.831	0.011
Total	7.999	7.998	6.829	7.726	7.685	4.987
Alm	62.4	75.6				
Sps	1.1	9.0				
Prp	27.0	10.6				
Grs	9.5	5.8				
X_{Mg}	0.30	0.12	0.56	0.78	0.42	

Note: Atoms per formula unit (apfu) caluclated on the basis of 12 O atoms (O) for garnet (Grt), 11 O atoms for phengite and biotite (Phg, Bt), and 8 O atoms for plagioclase (Pl).

TABLE 2. Whole-rock composition of sample P06

Major Elements (wt% oxides)		Trace Elements (ppm)			
SiO_2	56.81	Ba	744	Ce	50
TiO_2	1.02	Rb	173	La	27
Al_2O_3	21.52	Sr	138	Nd	24
$Fe_2O_{3\ total}$	7.97	Pb	19	Y	40
MnO	0.11	Th	13	Co	15
MgO	2.18	U	2	V	191
CaO	0.70	Cr	121	Zn	104
Na_2O	0.65	Zr	210	Nb	19
K_2O	4.23	Ni	56		
P_2O_5	0.20	Ga	26		
SO_3	0.03				
F	0.04				
LOI	3.64	LOI = Loss on ignition			
Total	99.10	La/Nd = 1.1			

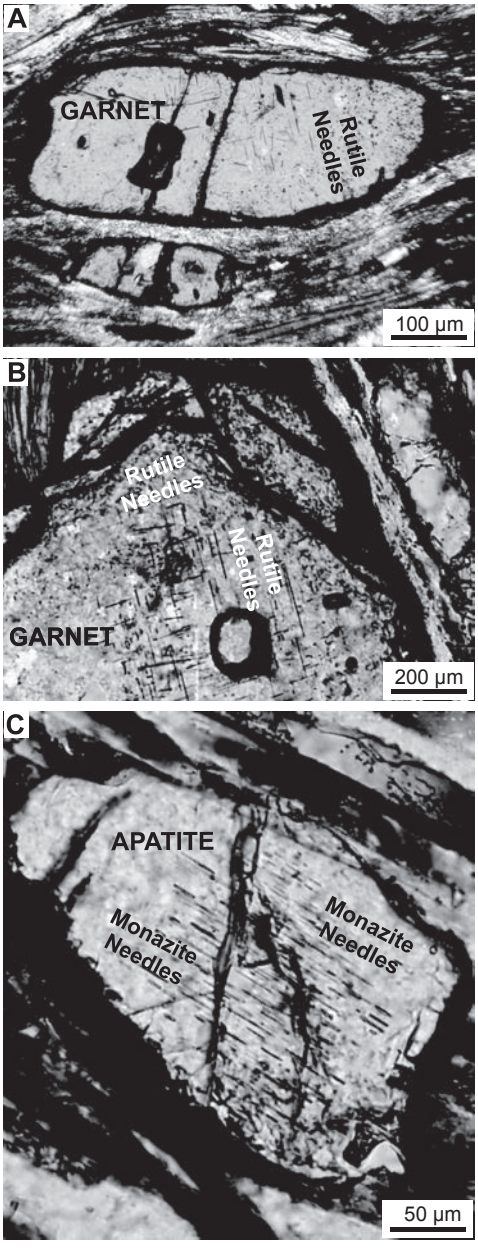

FIGURE 2. Photomicrographs (plane-polarized light) showing garnet porphyroblasts with rutile needles (**a**, **b**) and a large apatite grain containing abundant monazite needles (**c**).

with a Bruker S4 Pioneer WD spectrometer housed at Salzburg University. Major and trace elements were determined on glass beads and powders pellets, respectively (Table 2). The rock has a strongly peraluminous, Na_2O- and CaO-poor, and K_2O-rich pelitic composition. The LREE contents are 27 ppm La, 50 ppm Ce, and 24 ppm Nd. The La/Nd ratio is 1.1, and the Y content is 40 ppm.

P-T evolution

The *P-T* evolution of the investigated gneiss was reconstructed from textural relationships, phase equilibrium modeling, and thermobarometry (Fig. 3). A *P-T* pseudosection was calculated using the Perple_X thermodynamic software (Connolly 2005; version 07) with the internally consistent thermodynamic data set of Holland and Powell (1998; updated 2002). Stable assemblages were constrained from the whole-rock composition (Table 2) in the system Na_2O-CaO-K_2O-FeO-MgO-MnO-Al_2O_3-SiO_2-H_2O with water in excess (saturated phase). Based on the H_2O-rich composition of fluid inclusions with only minor CO_2 and CH_4 (Hurai et al. 2008), an aqueous fluid with unit activity of H_2O was used in the phase equilibrium calculations. Solid-solution models for garnet, staurolite, biotite, and phengite are those of Holland and Powell (1998), whereas that of plagioclase is from Newton et al. (1980) as available from the Perple_X datafile (solut_07.dat, http://www.perplex.ethz.ch/perplex/datafiles/solut_07.dat).

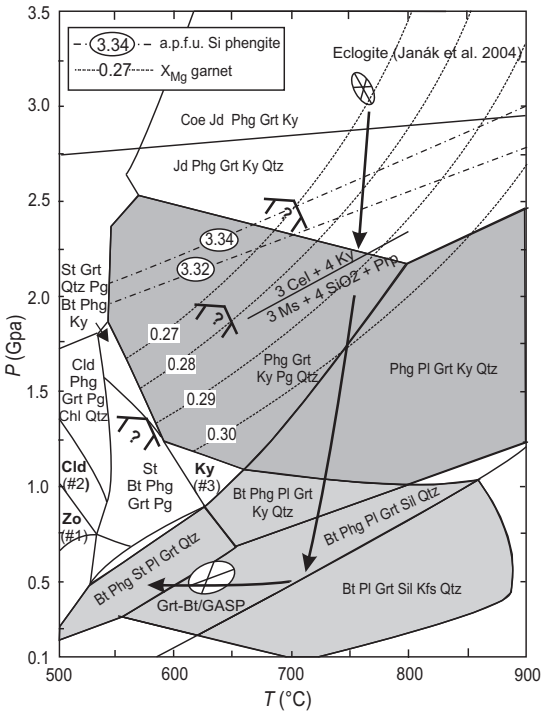

FIGURE 3. *P-T* pseudosection for the kyanite-garnet gneiss (sample P06) in the MnNCKFMASH system calculated using the Perple_X thermodynamic software of Connolly (2005, version 07). Gray-shaded areas correspond to the observed assemblages. Results of geothermobarometry are shown for gneiss and neighboring eclogites (Janák et al. 2004). Inferred *P-T* evolution of the gneiss is indicated by arrows. The isopleths of X_{Mg} in garnet and of Si (apfu) in phengite (Phg) are also shown. 1 = Zoisite-bearing mineral assemblage Zo-Cld-Bt-Phg-Grt-Pg (paragonite)-Chl-Qtz. 2 = Chloritoid-bearing assemblage Cld-Bt-Phg-Grt-Pg-Chl-Qtz. 3 = Kyanite-bearing assemblage Ky-Bt-Phg-Grt-Pg-Qtz. See text for further explanation. Mineral abbreviations after Kretz (1983).

The prograde path of the metamorphic evolution is difficult to assess because of the absence of prograde zoning in the chemically homogeneous garnet cores. Potential low *P-T* phases like chlorite, chloritoid, and zoisite (as inferred from the modeled pseudosection; Fig. 3) were probably decomposed completely during prograde metamorphism. Staurolite, kyanite, rutile, and Mg-rich biotite inclusions in garnet porphyroblasts are remnants from the prograde metamorphism.

According to the modeled *P-T* pseudosection, the peak metamorphic assemblage was garnet, kyanite, phengite, rutile, quartz or coesite, and jadeite-rich clinopyroxene (Fig. 3). To determine the pressure conditions from the observed assemblage garnet-kyanite-phengite-quartz/coesite, we used the equilibrium:

3 celadonite + 4 kyanite = 3 muscovite + 4 SiO_2 + pyrope,

calibrated as a geobarometer by Krogh Ravna and Terry (2004). The compositions of matrix phengite with maximum Si value and garnet cores yield 2.0–2.3 GPa at an assumed temperature of 700–800 °C (Fig. 3). Calculated isopleths from the measured garnet cores (X_{Mg} = 0.27–0.28) and matrix phengite (3.32–3.34 Si apfu) compositions intersect at 2.5–2.7 GPa (Fig. 3) according to the modeled *P-T* pseudosection. Since the gneiss samples were taken <100 m from a well-studied UHP-eclogite body (Janák et al. 2004), it is likely that they have experienced the same peak metamorphic conditions of ca. 3 GPa and 760 °C.

The retrograde growth of biotite, K-feldspar, and plagioclase in the matrix, coupled with a partial transformation of kyanite to sillimanite, indicates a nearly isothermal decompression of the rock down to ca. 0.5–0.6 GPa at T > 700 °C. Jadeite and coesite were most likely decomposed completely to white mica, plagioclase, and quartz. Subsequent cooling led to the formation of late staurolite in the matrix. *P-T* conditions for the retrograde stage have been calculated from the garnet-biotite geothermometer (calibration of Ferry and Spear 1978, with garnet model of Berman 1990), and the garnet-plagioclase-Al_2SiO_5 (GASP) geobarometer (Koziol and Newton 1988) using the re-equilibrated garnet rim and associated biotite and plagioclase compositions. The results suggest that cooling occurred at a minimum pressure of 0.4–0.5 GPa (Fig. 3), which is also consistent with isochores calculated from fluid inclusions (Hurai et al. 2008).

Monazite types

Based on the microstructural relationships observed in backscattered electron (BSE) images and a large set of microprobe analyses (analysis routine of Krenn and Finger 2007; see also Krenn et al. 2008), two contrasting monazite types have been distinguished in the gneiss. These are referred to hereafter as the M1 and M2 types.

Monazite of the first type (M1) forms as large and chemically homogenous grains (Figs. 4a and 5). They are characterized by a La/Nd ratio of 1.2–1.4, which is higher than that of the whole rock (~1.1 La/Nd). ThO_2 contents are in the range of 5–7 wt% (Fig. 5; Table 3). Y_2O_3 values are very low (<0.3 wt%), although the Y content of the whole rock is as high as 40 ppm.

The second type of monazite (M2) is chemically distinct from M1 monazite. It shows lower ThO_2 values (0.1–5 wt%) and unusually low La/Nd ratios (~0.3–0.9), which are significantly lower than the La/Nd whole-rock value (Fig. 5). The contents of MREEs are relatively higher than in M1 (3–5 wt% Sm_2O_3, 1.3–4.5 wt% Gd_2O_3; Fig. 5). The yttrium content of M2 monazite is variable (0.2–3.2 wt% Y_2O_3), but on average much higher than in M1. Since M2 monazite with ThO_2 > 1 wt% invariably has Y_2O_3 content greater than 1.8 wt%, there is a very clear separation of M1 and M2 monazite in the ThO_2 vs. Y_2O_3 diagram (Fig. 5).

Based on microtextural and morphological characteristics, M2 monazite grains can be classified into four subtypes. A first subtype (M2-a) forms tiny needles within matrix-apatite (Figs. 4b and 4c). Several, but not all, apatite grains in the rock display this feature. The highest concentration of monazite needles is found within the interiors of larger apatite crystals (Fig. 4b). Apatite enclosed in garnet is mostly devoid of such small monazite inclusions or shows at best very few of them (Fig. 4d). The M2-a monazite needles exhibit a general orientation parallel to the c-crystallographic axis of the host apatite.

Other matrix apatite is free of monazite needles but is rimmed by monazite (subtype M2-b; Fig. 4e). These M2-b grains form an integral part of the host apatite. Their composition is very

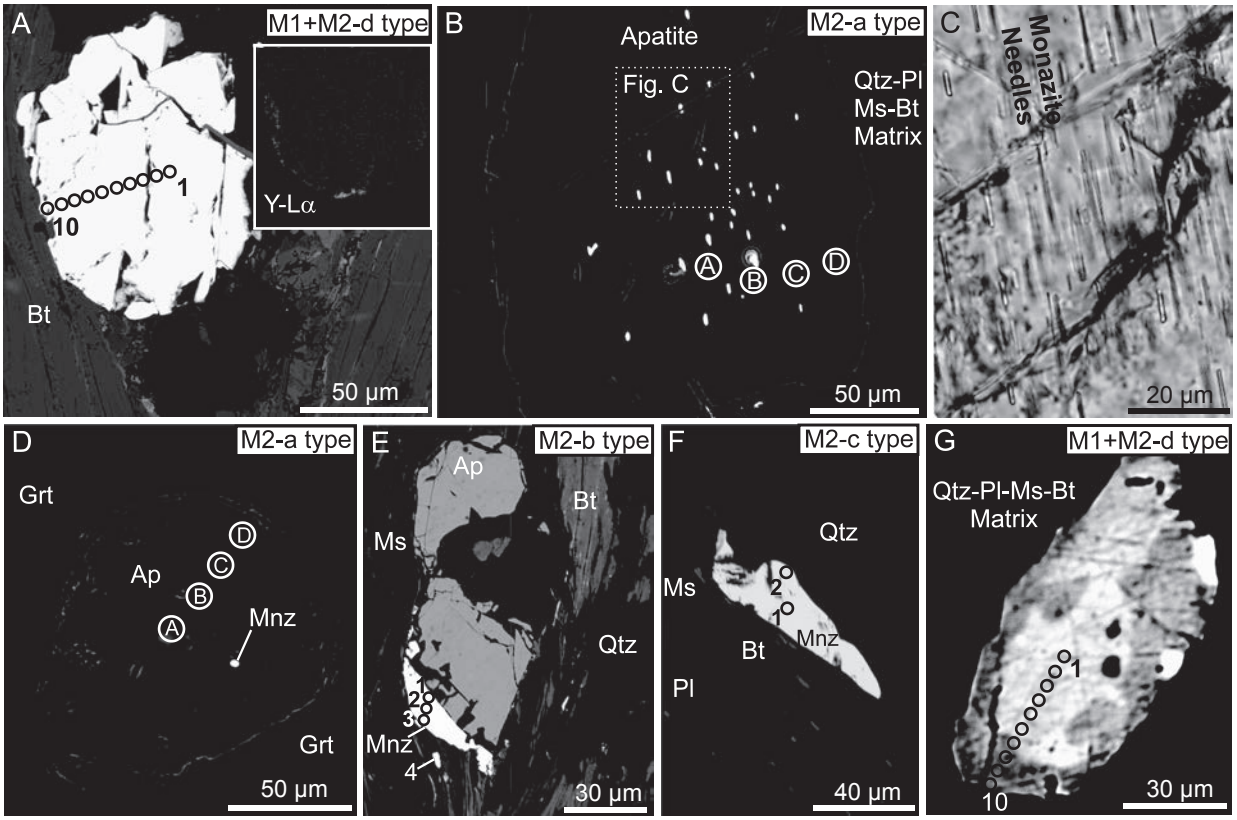

Figure 4. Back-scattered electron (BSE) images of monazite (Mnz) and apatite (Ap) grains from sample P06. (**a**) Large M1 monazite with thin, Y-rich M2-d rim domains. The Y contrast between M1 and M2-d rim domains is highlighted in the yttrium X-ray map in the inset. X-ray scan parameters were: 15 kV accelerating voltage, 100 nA cup current, 2400 × 1600 pixel resolution, and 4 s dwell time/line. (**b**) Large matrix apatite with tiny M2-a monazite inclusions. (**c**) Photomicrograph (plane-polarized light) of the center of the same apatite documenting lamellar orientation of the monazite inclusions. (**d**) Apatite shielded in garnet contains one small M2-a monazite inclusion. (**e**) M2-b monazite occurring at the rim of apatite. (**f**) Discrete M2-c matrix monazite. (**g**) Composite monazite with a bright M1 core and a broad, dark M2-d rim domain. Circles indicate the positions of microprobe analyses listed in Table 3 and of chemical profiles shown in Figures 6 and 8.

similar to the M2-a monazite needles (low Th, low La/Nd ratio; see Fig. 5 and Table 4). Some M2-b monazite grains exhibit Y zonation, with strong Y increase from core to rim (Fig. 4e, Table 3). Small monazite grains that nucleated slightly apart from the apatite (Fig. 4e) have the same composition as M2-b rim grains (Table 3).

A third textural subtype of M2 monazite (M2-c) occurs as subhedral, discrete grains (<50 µm) within the mica-rich matrix (Fig. 4f). Although most of these grains are not in contact with apatite, a genetic kinship with M2-a,b subtypes is expressed by the low La/Nd ratios. However, M2-c monazite grains tend to have higher ThO_2 and Y_2O_3 contents relative to the M2-a and M2-b subtypes (see Fig. 5).

Finally, a fourth textural subtype of M2 monazite (M2-d) occurs as overgrowths around M1 matrix monazite (Figs. 4a and 4g). These overgrowths may be only several micrometers thick as is highlighted by the X-ray scan shown as an inset in Figure 4a, or may be thicker in other cases (~20–30 µm; Fig. 4g). Contacts between the M1 core zone and the M2 rim zone are embayed and irregular, but discrete (see Fig. 4g). An affiliation of M2-d with the M2 monazite type can be inferred from its low La/Nd ratios. Like the isolated M2-c matrix monazites, the M2-d monazite subtype also displays higher Th and Y contents relative to the M2-a and M2-b subtypes.

Chemical profiles across zoned M1/M2 monazite grains (Figs. 6a and 6b) highlight the chemical differences between these two domains. The M1 domain is broadly homogenous, with high La/Nd ratios (>1.24) and very low Y values (<0.18 wt% Y_2O_3), as is typical for M1 monazite in general. However, the M2 domain shows much lower La/Nd ratios and higher Y_2O_3 values (up to ~2.4%; Figs. 6a and 6b). Table 4 provides a summary overview on the morphological appearance, textural setting, and chemical compositions of monazite M1 and monazite M2 (including subtypes).

Chemical Th-U-Pb monazite dates

The large M1 grain illustrated in Figure 4a was dated using the Cameca SX-100 electron microprobe in Bratislava via the analysis routine described in Konečný et al. (2004). The zoned M1 grain illustrated in Figure 4g, as well as other M1 and M2 monazite grains, were dated using a JEOL JX8600 microprobe housed at Salzburg University. Details of the analysis routine and analytical settings are given in Krenn et al. (2008).

Table 5 lists the Th, U, and Pb abundances of monazite, as

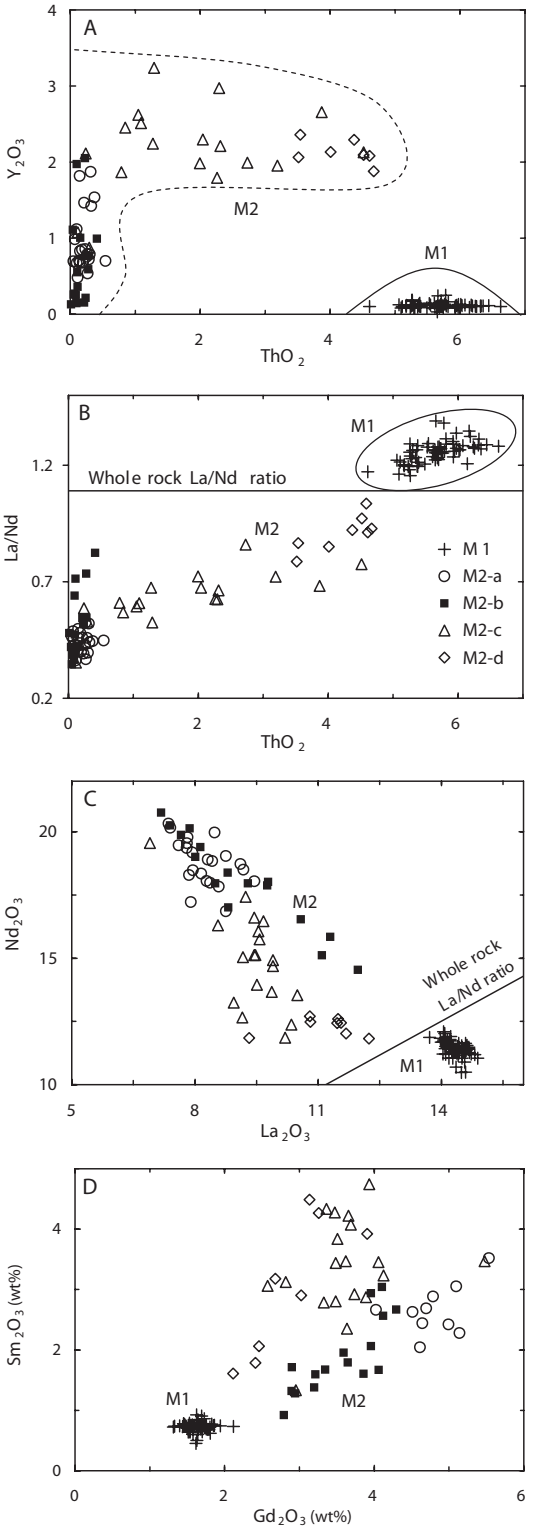

FIGURE 5. Compositional variation of monazite in the kyanite-garnet gneiss from the Pohorje Mountains. The different monazite types are shown with different symbols. Two-sigma errors are maximally ±0.07 wt% for Y_2O_3, ±0.11 wt% for La_2O_3 and Nd_2O_3, and ±0.06 wt% for ThO_2. Details pertaining to analytical settings are given in Krenn and Finger (2007) and Krenn et al. (2008).

well as the corresponding chemical dates and their ±2σ uncertainties. Ages and errors were calculated after the method of Montel et al. (1996) considering the 2σ errors of Th (0.025 wt%), U (0.023 wt%), and Pb (0.009 wt%) abundances, which were determined at 15 kV accelerating voltage, 150 nA beam current, and counting times of 40 s for U and Th and 320 s for Pb. Also shown are the weighted-mean dates, which were calculated by internal error propagation at a 2σ confidence level using the

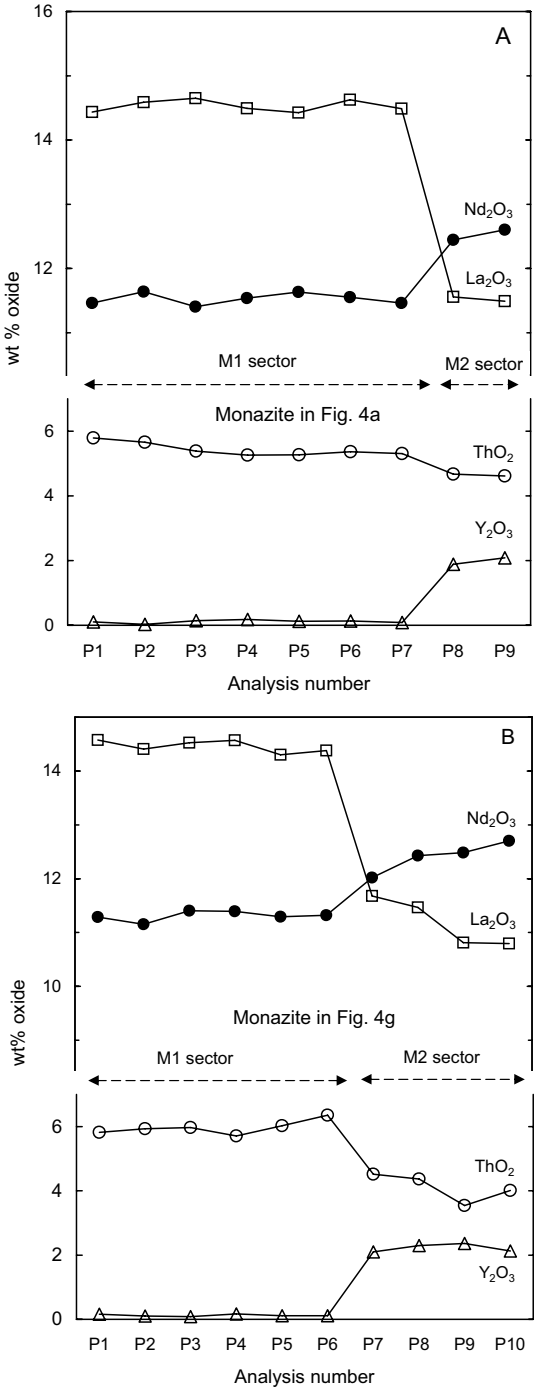

FIGURE 6. Chemical profiles across the composite M1/M2-d monazite grains shown in Figures 4a and 4g.

TABLE 3. Electron microprobe analyses of monazite and apatite from the kyanite-garnet gneiss

Mineral	M1	M1	M1	M2-a	M2-a	M2-b	M2-b	M2-b	M2-b	M2-c	M2-c	M2d	M2-d	M2-d	Ap	Ap	Ap	Ap
Figure	4a/1	4a/2	4g/1	4b	–	4e/1	4e/2	4e/3	4e/4	4f/1	4f/2	4a/10	4g/9	4g/10	4b/A	4b/D	4d/A	4d/D
SiO_2	0.26	0.33	0.37	0.00	0.05	0.03	0.03	0.03	0.12	0.12	0.08	0.24	0.38	0.31	0.03	0.05	0.06	0.05
P_2O_5	28.59	28.61	29.38	30.14	30.05	30.29	30.08	30.84	30.36	29.99	29.58	28.63	30.07	30.04	41.05	41.23	41.34	40.93
CaO	1.13	1.07	0.90	0.00	0.00	0.21	0.02	0.21	0.22	0.47	0.20	0.99	0.52	0.46	53.70	54.06	54.45	54.04
Y_2O_3	0.08	0.13	0.11	0.68	0.75	0.15	0.27	0.99	2.11	1.79	3.24	1.88	2.29	2.36	0.19	0.20	0.09	0.08
La_2O_3	14.49	14.62	14.41	7.80	7.95	10.58	6.87	11.97	9.66	9.06	8.56	11.55	9.63	8.94	<d.l.	0.025	0.020	0.023
Ce_2O_3	30.68	31.15	31.84	29.27	29.50	33.37	30.69	30.91	29.31	28.58	26.85	28.70	27.48	28.40	0.07	0.07	0.09	0.07
Pr_2O_3	3.13	3.40	3.01	3.54	3.93	3.97	4.15	3.58	3.38	3.37	3.46	3.38	2.89	3.01	<d.l.	<d.l.	<d.l.	<d.l.
Nd_2O_3	11.46	11.55	11.15	19.54	18.48	16.54	20.46	14.54	16.46	15.58	16.29	12.44	13.48	13.80	0.08	0.09	0.06	0.05
Sm_2O_3	1.68	1.54	1.58	4.99	4.69	2.79	4.06	2.90	4.06	3.48	3.93	2.41	3.14	3.26	0.07	0.10	0.10	0.07
Gd_2O_3	0.69	0.64	0.60	2.42	2.69	0.92	1.67	1.71	3.46	3.51	4.74	1.79	4.49	4.27	<d.l.	<d.l.	<d.l.	<d.l.
Dy_2O_3	0.03	0.04	0.15	0.39	0.32	0.18	0.13	0.32	0.69	0.74	1.15	0.47	0.81	0.71	<d.l.	<d.l.	<d.l.	<d.l.
Er_2O_3	<d.l.	<d.l.	<d.l.	<d.l.	<d.l.	0.12	<d.l.	0.32	0.15	0.15	0.29	0.00	0.37	0.33	<d.l.	<d.l.	<d.l.	<d.l.
ThO_2	5.30	5.37	5.93	0.20	0.26	0.09	0.06	0.41	0.24	2.26	1.29	4.67	4.37	3.54	<d.l.	<d.l.	<d.l.	<d.l.
UO_2	0.68	0.67	0.57	0.26	0.21	0.44	0.41	0.65	0.51	0.66	0.54	0.33	0.48	0.38	<d.l.	<d.l.	<d.l.	<d.l.
PbO	0.03	0.03	0.03	0.01	0.04	0.03	0.01	0.03	0.03	0.00	0.03	0.03	0.01	0.02	<d.l.	<d.l.	<d.l.	<d.l.
Cl	n.d.	n.d.	n.d.	n.d.	n.d.	n.d.	n.d.	n.d.	n.d.	n.d.	n.d.	n.d.	n.d.	n.d.	<0.02	<0.02	<0.02	<0.02
F	n.d.	n.d.	n.d.	n.d.	n.d.	n.d.	n.d.	n.d.	n.d.	n.d.	n.d.	n.d.	n.d.	n.d.	3.29	3.55	3.49	3.65
Total	98.24	99.16	100.03	99.25	98.92	99.71	98.92	99.42	100.77	99.75	100.24	97.54	100.42	99.83	97.09*	97.88	98.24	97.42
La/Nd	1.26	1.27	1.29	0.40	0.43	0.64	0.34	0.82	0.59	0.58	0.53	0.93	0.71	0.65				
Si (apfu)	0.010	0.013	0.015	0.000	0.002	0.001	0.001	0.001	0.005	0.005	0.003	0.010	0.015	0.012	0.003	0.005	0.005	0.005
P	0.990	0.990	0.990	1.006	1.005	0.990	1.006	0.990	0.990	0.996	0.990	0.990	0.992	0.993	0.990	0.990	0.990	0.990
Ca	0.049	0.046	0.038	0.000	0.000	0.009	0.001	0.009	0.009	0.020	0.008	0.043	0.022	0.019	4.968	4.969	4.987	4.996
Y	0.002	0.003	0.002	0.014	0.016	0.003	0.006	0.021	0.044	0.037	0.068	0.040	0.048	0.049	0.009	0.009	0.004	0.004
La	0.216	0.217	0.210	0.113	0.116	0.153	0.100	0.172	0.138	0.131	0.124	0.172	0.138	0.129	0.000	0.001	0.001	0.001
Ce	0.453	0.458	0.461	0.423	0.427	0.479	0.444	0.440	0.416	0.411	0.387	0.424	0.392	0.406	0.002	0.002	0.003	0.002
Pr	0.046	0.050	0.043	0.051	0.057	0.057	0.060	0.051	0.048	0.048	0.050	0.050	0.041	0.043	–	–	–	–
Nd	0.165	0.166	0.157	0.275	0.261	0.232	0.289	0.202	0.228	0.218	0.229	0.179	0.188	0.193	0.003	0.003	0.002	0.001
Sm	0.023	0.021	0.022	0.068	0.064	0.038	0.055	0.039	0.054	0.047	0.053	0.034	0.042	0.044	0.002	0.003	0.003	0.002
Gd	0.009	0.009	0.008	0.032	0.035	0.012	0.022	0.022	0.044	0.046	0.062	0.024	0.058	0.055	0.001	0.005	0.000	0.000
Dy	0.000	0.001	0.002	0.005	0.004	0.002	0.002	0.004	0.009	0.009	0.015	0.006	0.010	0.009	0.000	0.000	0.000	0.000
Er	–	–	–	–	–	0.001	–	0.004	0.002	0.002	0.004	–	0.005	0.006	–	–	–	–
Th	0.049	0.049	0.053	0.000	0.000	0.001	0.000	0.004	0.002	0.000	0.012	0.043	0.000	0.000	–	–	–	–
U	0.006	0.006	0.005	0.002	0.002	0.004	0.001	0.006	0.004	0.020	0.005	0.003	0.039	0.031	–	–	–	–
Pb	0.000	0.000	0.000	0.002	0.002	0.000	0.004	0.000	0.000	0.006	0.000	0.000	0.004	0.003	–	–	–	–
tetr.	1.000	1.003	1.004	1.006	1.007	0.991	1.008	0.991	0.994	1.001	0.993	0.999	1.007	1.006	0.992	0.994	0.995	0.994
[9]	1.019	1.025	1.002	0.985	0.983	0.991	0.983	0.971	0.997	0.995	1.015	1.018	0.986	0.988	4.985	4.992	4.999	5.006

Notes: M1 = M1 monazite, M2 = M2 monazite, Ap = apatite, n.d. = not determined, d.l. = detection limit. Stoichiometry of monazite and apatite calculated on the basis of 4 and 12.5 O atoms.
* –O = F.

TABLE 4. Monazite types in the studied sample

Type	Shape and textural setting	Size (μm)	La/Nd	ThO_2	Y_2O_3
M1	Subhedral grains in the matrix	30–300	1.2–1.4	5–7	<0.25
M2-a	Monazite needles within apatite	<1–10	<0.5	<0.5	0.5–1.8
M2-b	Monazite crystals at the rims of apatite and in the closer proximity to apatite	<1–30	0.3–0.8	<0.5	0.2–2.1
M2-c	Subhedral grains in the matrix	20–50	0.6–0.8	1–4.5	1.5–3.3
M2-d	Monazite seams around M1 monazite	5–30	~0.9	3.5–4.5	~2

Isoplot program (Ludwig 2001, v. 2.49e).

Forty-four analyses of the large M1 grain shown in Figure 4a define a weighted average date of 98 ± 8 Ma (±2σ error; MSWD = 1.2; Table 5). The inner, low-Y domain of M1 monazite in Figure 4g yields a weighted mean date of 107 ± 16 Ma (MSWD = 1.6). Other M1 monazite grains analyzed during this study provide a date of 105 ± 14 Ma (MSWD = 1.2). The entire M1 population provides a weighted mean date of 100 ± 6 Ma (MSWD = 1.6). For M2 monazite, a weighted mean date of 71 ± 15 Ma (MSWD

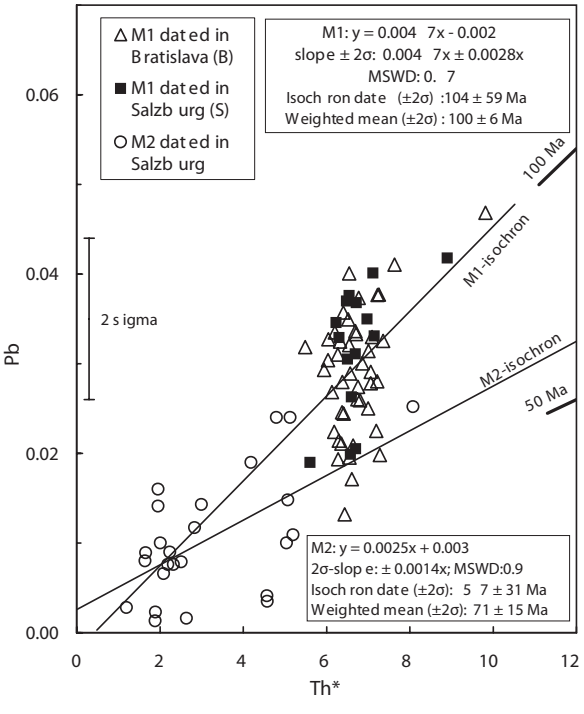

► **FIGURE 7.** Th* vs. Pb diagram after Suzuki et al. (1991). Shown are the isochrons through M1 and M2 monazite, slope and intersection values of isochrons, the 2σ errors on the isochron slope (M1: 0.0047x ± 0.0026x; M2: 0.0025x ± 0.0014x), and the MSWD values. Also highlighted are the isochron dates (±2σ) and the weighted mean dates (±2σ). See text for details concerning age and error calculations. Age bars (100 Ma, 50 Ma) on the right side of the margin are zero-intersecting isochrons.

TABLE 5. Results of chemical dating of M1 and M2 monazite

Th	U	Pb	Th*	Date	±2σ	Th	U	Pb	Th*		Date	±2σ
M1 monazite dated in Bratislava (Grain A in Fig. 4)						M1 monazite dated in Salzburg (Grain G, Fig. 4 continued)						
5.045	0.490	0.017	6.607	58	34	5.249	0.545	0.029	6.989		92	34
4.475	0.487	0.030	6.033	114	37	5.017	0.536	0.026	6.729		86	35
4.050	0.448	0.032	5.485	131	41	5.299	0.437	0.031	6.694		105	35
5.042	0.340	0.027	6.128	99	37	5.584	0.478	0.040	7.115		127	33
7.426	0.748	0.047	9.817	108	23	5.252	0.455	0.021	6.703		69	35
5.497	0.540	0.028	7.221	88	31	5.080	0.511	0.037	6.717		123	35
5.401	0.581	0.038	7.260	117	31	4.974	0.393	0.035	6.233		125	38
5.285	0.539	0.031	7.010	101	32	Weighted mean date: 106 ± 16 Ma (MSWD: 1.5)						
5.110	0.494	0.034	6.691	113	34							
5.440	0.517	0.033	7.094	105	32	Other M1 monazite dated in Salzburg						
5.661	0.531	0.033	7.358	100	31	4.623	0.600	0.038	6.544		129	36
5.422	0.512	0.029	7.060	93	32	4.447	0.362	0.019	5.601		76	42
5.550	0.543	0.020	7.280	61	31	7.462	0.450	0.042	8.901		106	26
5.481	0.536	0.023	7.191	71	31	4.660	0.601	0.020	6.578		68	36
4.927	0.317	0.029	5.941	111	38	4.715	0.590	0.026	6.599		90	36
5.207	0.500	0.026	6.802	86	33	4.626	0.523	0.033	6.299		118	37
5.822	0.565	0.041	7.630	121	30	4.619	0.590	0.031	6.507		106	36
5.002	0.482	0.040	6.547	138	34	4.727	0.549	0.037	6.485		129	36
4.727	0.524	0.036	6.405	126	35	4.966	0.627	0.035	6.971		113	34
4.720	0.520	0.028	6.380	99	35	5.088	0.643	0.033	7.143		104	33
4.967	0.559	0.027	6.752	92	33	Weighted mean date: 105 ± 14 Ma (MSWD: 1.2)†						
4.598	0.524	0.031	6.274	111	36							
4.648	0.525	0.032	6.328	116	36	M2 monazite dated in Salzburg						
4.994	0.548	0.026	6.743	87	33	0.211	0.527	0.001	1.885	‡	16	97
5.210	0.559	0.025	6.994	81	32	0.187	0.552	0.014	1.960	‡	163	93
5.026	0.481	0.029	6.564	99	34	0.201	0.592	0.007	2.091	‡	72	87
4.825	0.537	0.032	6.543	110	34	0.137	0.470	0.008	1.641	‡	111	111
4.990	0.556	0.037	6.771	124	33	0.245	0.441	0.009	1.658	‡	122	110
4.960	0.526	0.021	6.640	71	34	0.364	0.572	0.008	2.191	‡	79	83
4.699	0.524	0.025	6.374	87	35	0.240	0.535	0.016	1.960	‡	185	93
4.739	0.524	0.024	6.412	86	35	0.077	0.351	0.003	1.195	‡	53	153
4.546	0.514	0.022	6.187	82	36	0.102	0.597	0.010	2.012	‡	113	101
4.542	0.545	0.019	6.281	69	36	0.258	0.514	0.002	1.892	‡	28	108
4.614	0.546	0.021	6.358	75	35	2.032	0.303	0.014	2.999	§	108	68
4.489	0.486	0.033	6.047	122	37	7.046	0.325	0.025	8.081	§	70	25
4.627	0.522	0.021	6.292	77	36	3.968	0.362	0.024	5.125	§	106	40
4.858	0.520	0.035	6.524	121	35	1.135	0.473	0.002	2.638	§	14	77
4.873	0.490	0.013	6.432	46	35	0.742	0.495	0.008	2.321	§	74	88
5.009	0.531	0.033	6.706	112	34	0.956	0.402	0.009	2.240	§	91	91
4.935	0.507	0.020	6.553	67	34	0.923	0.499	0.008	2.514	§	71	81
5.226	0.509	0.030	6.853	99	33	3.400	0.370	0.004	4.575	§	20	44
5.340	0.538	0.028	7.057	89	32	1.753	0.339	0.012	2.835	§	93	72
5.066	0.353	0.033	6.198	122	36	4.030	0.328	0.015	5.075	§	66	40
5.556	0.522	0.038	7.225	118	31	3.523	0.331	0.004	4.576	§	17	44
Weighted mean date: 98 ± 7 Ma (MSWD: 1.6)						3.841	0.426	0.011	5.197	§	47	39
						3.111	0.337	0.019	4.188	§	102	48
M1 monazite dated in Salzburg (Grain G in Fig. 4)						4.050	0.234	0.024	4.798	§	113	42
5.113	0.488	0.030	6.674	101	35	4.105	0.293	0.010	5.038	§	45	40
5.211	0.504	0.039	6.825	127	34	Weighted mean date M2: 71 ± 15 Ma (MSWD: 2.0)						

Notes: Weighted mean date calculated by internal error propagation at a 2σ confidence level using the isoplot program 2.49e of Ludwig (2001). Weighted mean date of M2-a,b: 97 ± 40 Ma (MSWD: 1.2). Weighted mean date of M2-c,d: 66 ± 19 Ma (MSWD: 1.9).
† Weighted mean date of all M1 monazite: 100 ± 6 Ma (MSWD: 1.6).
‡ M2-a,b.
§ M2-c,d.

= 2.0) was obtained.

The geochronological monazite results are also presented in a Th* vs. Pb diagram (Fig. 7). The isochrons were calculated by means of the least-squares fitting method of York (1966), which accounts for the 2σ analytical errors of Th, U, and Pb. M1 monazite defines an isochron with a slope and related ±2σ error of 0.0047 (±0.0026), an intercept value of –0.002, and a MSWD value of 0.70. The isochron through M2 monazite has a slope of 0.0025 (±0.0014) and intersects the Y-axis at 0.0026. The MSWD value is 0.90. The isochron dates and related 2σ errors are 104 ± 59 Ma for M1 and 57 ± 31 Ma for M2, respectively. It is emphasized that the relatively high error on the M1 isochron results from its narrow Th* spread. The low Pb values in M2 monazite, which are close to or below the detection limit of 0.009 wt%, propagates the high uncertainties in the calculated M2 age. For the Pb aquisition an exponential background model was used to provide maximal Pb counts (see Jercinovic and Williams 2005; Krenn et al. 2008).

The EMPA dates for M1 monazite are consistent with published Sm-Nd garnet dates (93–97 Ma) and U-Pb zircon dates (91–92 Ma) from gneisses and eclogites of Pohorje (Thöni 2002; Miller et al. 2005; Cornell et al. 2007). These ages record the high-pressure event in this area. Although the EMPA monazite dates presented here provide insufficient information regarding the age difference between M1 and M2, they are nonetheless important inasmuch as they show that monazite grains in this rock grew during Alpine metamorphism and are not older relics (e.g., detrital or inherited) from pre-Alpine orogeny.

Apatite and xenotime

A systematic microprobe study of the apatite was undertaken using the analysis routine of Krenn and Finger (2004). The apatite grains always appear homogeneous and unzoned in BSE images (Figs. 4b, 4d, and 4e), irrespective of whether or not they carry M2-a monazite inclusions. Also, microprobe analyses did not reveal systematic chemical differences between apatites with or without monazite inclusions. Both are nearly pure Ca-F apatite with only low trace-element contents (Table 3). Only small amounts of Y_2O_3 (0.1–0.25 wt%) and Nd_2O_3 (~0.1 wt%) were detected, whereas La_2O_3 and Ce_2O_3 abundances were found to be below detection limits (<0.09 wt%). Element distributions within single apatite grains are generally flat with no significant zoning observed (Fig. 8). However, apatite inclusions in the garnet are systematically lower in Y_2O_3 (<0.1 wt% Y_2O_3) than the matrix apatite (0.14–0.25 wt%).

Several small grains of xenotime have also been found in thin section P06. All grains occur in the secondary matrix in close proximity to garnet and Y-rich M2 monazite types. Xenotime strongly resembles M2-c matrix monazite grains in shape and size. No xenotime was found within garnet.

Discussion

Two monazite types in the kyanite-garnet gneiss from Pohorje

The existence of two different monazite types (M1; M2) in the single rock investigated in this study is supported by their morphological and textural appearance as well as by their different chemical signatures (e.g., La/Nd and LREE/MREE ratios, Th and Y abundances, etc.). M2 monazite overgrowths on M1 monazite show that M2 formed during a later stage, consistent with the slightly younger Th-U-Pb dates of M2 relative to M1 monazite. The significant chemical, textural, and morphological differences further imply that the two monazite types formed by different reactions and from different REE sources.

For M1, there is no clear microstructural evidence with regard to its formation history. In the case of M2 monazite, however, microstructural observations in thin-section imply that apatite was an important reactant. Specifically, the needle-like, oriented inclusions of M2-a monazite in apatite, and the parasitic M2-b monazite grains at apatite margins support this interpretation. Moreover, trace-element patterns of apatite typically display high REE/Th ratios and both Nd- and MREE-enrichment (relative to La), as is observed also in M2 monazite (cf. Watson and Green 1981; Fleet and Pan 1997). It seems clear from these observations that M2-a and M2-b monazite grains grew directly from pre-existing apatite and derived its components almost exclusively therefrom. This process has also been confirmed by means of experiments. Indeed, Harlov and Förster (2002) and Harlov et al. (2005) showed that natural apatite, if LREE-rich, reacts to LREE-poor apatite plus monazite.

The growth of the larger M2-b grains on the rims of apatite (Fig. 4f) may have been supported by Ostwald ripening (e.g., Ayers et al. 1999), a process that led to the consumption of earlier formed small M2-a needles. This potentially explains why apatite grains with large M2-b rims never contain small M2-a monazite needles. Coarsening of monazite by Ostwald ripening has been recently documented by Hansen and Harlov (2006, 2007) in the case of parasitic monazite inclusions in apatite from Tamil Nandu, India. Monazite that nucleated close to M2-b rim grains, but slightly apart from the apatite (Fig. 4e; Table 3), has a similar composition to that of M2-b rim monazite and of monazite needles in apatite. This similarity suggests that these grains were derived from an apatite source as well, and that REEs were mobile on at least a small scale.

The M2-c monazite grains in the matrix have a low La/Nd ratio and therefore most probably also received chemical input from the apatite source, even though they are not in close proximity to the apatite. This further implies that the LREEs liberated from apatite did not always reprecipitate as monazite within or at the rim of the host apatite but instead were mobile on a small scale. The same can be inferred for the M2-d monazite subtype, which formed by a dissolution/reprecipitation process at the margins of M1 grains (Fig. 4). M2-d monazite has higher Th content relative to the M2-a and M2-b subtypes, which is probably derived from the M1 monazite. Likewise, it may be argued that some of the M2-c matrix monazite grains represent totally replaced former M1 monazite grains, because their Th contents are relatively high as well. Thus M2-c,d monazites are likely to contain components from the M1-monazite and an apatite source.

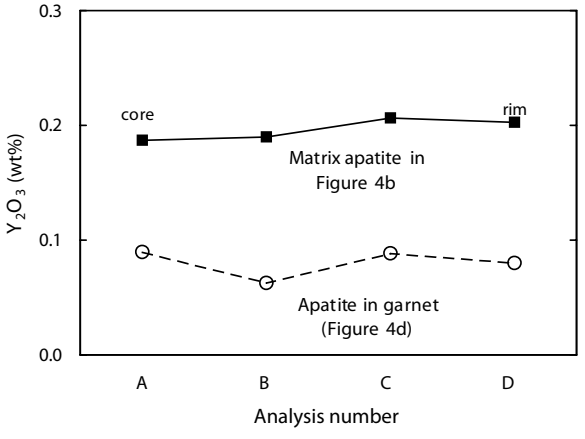

Figure 8. Yttrium distribution in apatite enclosed in garnet (Fig. 4d) and in matrix apatite with monazite inclusions (Fig. 4b).

Yttrium systematics of M2 monazite

Many of the M2-c monazite grains in the matrix show high Y_2O_3 contents, in the range of 2–3 wt%, as do the M2-d monazite overgrowths (see Figs. 5 and 6). The higher Y content in these grains relative to M2-a and M2-b subtypes is ascribed to the retrograde breakdown of garnet, which is an important Y carrier in metapelites (e.g., Zhu and O'Nions 1999; Pyle et al. 2001). Xenotime in the matrix also likely formed (during decompression) as a consequence of garnet breakdown and related Y liberation. There is wide agreement in literature (Foster et al. 2000, 2002; Pyle et al. 2001; Gibson et al. 2004; Finger and Krenn 2007; Jeřábek et al. 2008) that retrograde breakdown of garnet in high-grade rocks typically leads to a dramatic increase in yttrium activity and consequent precipitation of xenotime.

A modeled *P-T* pseudosection (Fig. 9) shows that garnet breakdown occurred close to the end of isothermal decompres-

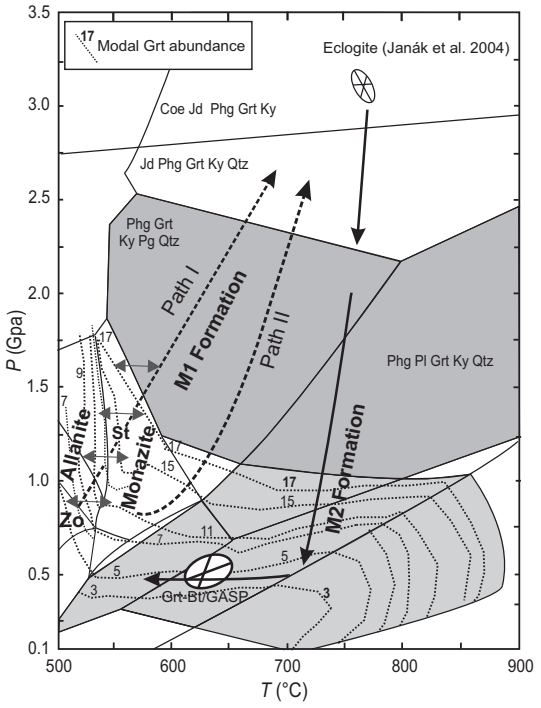

FIGURE 9. *P-T* pseudosection as in Figure 3, with garnet modal isopleths. The *P-T* range where allanite in metapelitic rocks with low CaO contents of ~0.5–1 wt% commonly reacts to monazite is outlined approximately with double-headed arrows. The proposed *P-T* areas for M1 and M2 monazite formation in the kyanite-garnet gneiss are indicated. I and II are hypothetical prograde *P-T* paths, which have different effects on prograde monazite growth. (See text for further explanations.) Mineral assemblages in field areas are the same as in Figure 3.

sion (at temperatures of ~700–800 °C), below a pressure of ~1 GPa. Matrix monazite formed during this high-*T* garnet breakdown should have acquired a high Y content due to the temperature-dependent YPO_4 exchange between monazite and xenotime (e.g., Heinrich et al. 1997). Application of the monazite-xenotime miscibility-gap thermometers (Heinrich et al. 1997; Gratz and Heinrich 1997; Pyle et al. 2001; Seydoux-Guillaume et al. 2002) to the M2 matrix monazites with the highest Y (apfu) and Y+HREE (apfu) contents of ~0.07 and 0.13, respectively (Table 3), indicate monazite formation temperatures of at least 700 °C. These inferred temperatures of formation suggest that M2 monazite growth occurred before the rock underwent isobaric cooling.

Even though M2-a and M2-b monazite types have, on average, lower Y values than M2-c and M2-d monazite types (Fig. 5; Table 3), the rimward Y increase in some of the larger M2-b rim grains (up to >2 wt% Y_2O_3; see analyses 4e/1–4 in Table 3) suggests that the Y availability increased during M2-b monazite growth. M2-a and M2-b monazite nuclei started to grow before abundant yttrium became available from garnet breakdown, i.e., during an earlier stage of decompression (Fig. 9), and proceeded to grow in a Y-richer environment during the stage of garnet consumption. Because of the high Y contents and the rimward Y increase in M2 monazite, it is not possible that M2 monazite formed along the prograde *P-T* path where garnet was a stable phase (see Figs. 3 and 9). It is also concluded that the formation of Y-undersaturated M2-a and M2-b nuclei was primarily triggered by the instability of a REE-enriched apatite during pressure decrease rather than by the breakdown of garnet and related Y release, respectively. Moreover, the generally high Y contents of M2-d monazite, on the other hand, which formed around and to some degree at expense of M1 monazite, suggest that excess Y liberated from garnet breakdown triggered the consumption of M1 monazite.

Parasitic monazite growth observed within apatite either represents a metasomatic reaction of apatite with an external fluid (Harlov et al. 2005) or is the result of solid-state diffusion. Microstructures indicative of a metasomatic reaction (e.g., contacts of reacted with unreacted crystal portions; cf. Harlov et al. 2005) have not been observed. These may have been obliterated by elevated REE-diffusion in apatite at high temperature (Cherniak and Ryerson 1993; Cherniak et al. 2004). From the example shown in Figure 4d, it appears difficult for LREE-rich external fluids to have penetrated apatite grains along cracks in the host garnet. If LREEs had reached the apatite, then yttrium, which is commonly more mobile than LREEs, should have reached the apatite as well. Yet, this is not the case. Instead, the Y contents of apatite enclosed in garnet are systematically lower than in the matrix apatite (Fig. 8). This is interpreted as evidence that formation of parasitic monazite at the expense of apatite can essentially operate in the absence of fluid. However, it is important to note that apatite inclusions in garnet are mostly devoid of monazite needles and monazite rims. Therefore, it is likely that the apatite enclosed in garnet was never as REE-rich as the apatite in the matrix.

Prograde monazite formation in the kyanite-garnet gneiss from Pohorje

In pelitic rocks undergoing prograde metamorphism, monazite often grows over a temperature range of ~500–600 °C, which according to results of Janots et al. (2007) roughly corresponds to the start of the monazite stability field and end of the allanite stability field, respectively. Indeed, numerous studies (Wing et al. 2003; Krenn and Finger 2007; Tomkins and Pattison 2007; Janots et al. 2008; Corrie and Kohn 2008) show that monazite formation in this amphibolite facies *P-T* range involves the breakdown of allanite. As demonstrated by phase equilibrium modeling (Figs. 3 and 9), the whole-rock composition of the monazite-bearing Pohorje metapelite is favorable for the stability of zoisite at *P-T* conditions of ~500 °C at 0.4–0.8 GPa. Because the stability field of allanite is similar to that of zoisite, it could be argued that allanite was also stable in the rock at an early stage of prograde metamorphism. Evidence is lacking for the presence of older monazite relics and therefore that the Cretaceous M1 monazite had formed from such remnants through dissolution and reprecipitation. Even the cores of the unusually large (~300 µm!) M1 monazite in Figure 4a provide Cretaceous dates while also indicating no chemical and morphological irregularities (e.g., embayments) in chemical traverses, element maps, and back-scattered electron images.

The precise location of the allanite-to-monazite reaction in the *P-T* space is difficult to constrain and might extend to slightly

higher temperatures at higher pressures (Wing et al. 2003; Janots et al. 2006, 2007). In Figure 9, the *P-T* range of the allanite-to-monazite reaction in metapelites is approximated according to results of Janots et al. (2007) for a bulk composition similar to that of the Pohorje gneiss (this study). Two possible paths for the prograde *P-T* evolution of this gneiss are shown in Figure 9. If the evolution followed path I in Figure 9, prograde monazite should have formed together with garnet in the Bt-Phg-St-Grt-Pg-Qtz field and in the Bt-Phg-Grt-Ky-Pg field. The modal garnet isopleths (Fig. 9) show that the main phase of garnet growth occurred at moderate pressures.

Coeval growth of garnet and M1 monazite is in conflict with following observations, which would imply that the M1 monazite grew after garnet: (1) Garnet in the rock is free of M1 monazite inclusions; (2) the Y content in M1 monazite is very low, although the whole-rock yttrium content of ~40 ppm would basically allow the formation of Y-rich monazite, as is evidenced by the high Y in M2 monazite types. This indicates that large amounts of garnet were already present when M1 monazite grew. The role of garnet as an important Y sink in high-grade metamorphic rocks has been demonstrated in many previous studies (Zhu and O'Nions 1999; Pyle and Spear 1999; Pyle et al. 2001). And (3) if monazite grew contemporaneously with garnet, a Y decrease from monazite cores to monazite rims could be expected (e.g., Pyle and Spear 2003). However, this is not observed in the Pohorje gneiss, in which M1 monazite lacks such Y zoning. Instead, therefore, it is hypothesized that prograde *P-T* evolution of this rock followed path II in Figure 9. In this case, the allanite would have reacted to monazite at higher pressures, well within the Phg-Grt-Ky-Qtz field and essentially after the main phase of garnet growth. Path II would also cross staurolite- and kyanite-bearing fields (see Figs. 3 and 9), consistent with the staurolite and kyanite inclusions observed in garnet.

A genetic fingerprint of M1 monazite is its high La/Nd ratio, which is significantly higher than that of the whole rock (Fig. 5). This chemical signature requires that during M1 monazite growth another LREE carrier mineral with a La/Nd ratio much lower than that of the whole rock was present in significant quantities. Judging from the secondary parasitic M2 monazite in and around apatite, this low La/Nd phase was most probably a REE-rich apatite stable at elevated pressure conditions. That apatite can be stable at ultrahigh-*P* conditions of >10 GPa has been confirmed by means of experiments (e.g., Murayama et al. 1986). Moreover, it was found that the lattice parameters of apatite decrease slightly with increasing pressures (Matsukage and Ono 2004). This decrease should favor incorporation of the smaller MREEs relative to the larger LREEs and should favor higher La/Nd ratio in apatite and in monazite crystals that grew parasitically from apatite. Other REE- and P-bearing phases, such as bearthite [$Ca_2Al(PO_4)_2(OH)$], have also been reported from metapelitic high-pressure rocks (e.g., Scherrer et al. 2001; Chopin and Ferraris 2003). We cannot rule out that such a REE-bearing phosphate phase was present in the studied sample at peak pressure, and then reacted back to monazite and apatite. However, since there is no textural evidence for this (e.g., no pseudomorphs), we infer that during the high-*P* stage a considerable portion of the REEs were trapped in the apatite and released later during the decompression stage.

Coeval growth of M1 monazite and REE-enriched high-*P*-apatite is likely in view of the widely homogeneous and constantly La-rich composition of the M1 monazite grains (Fig. 6b). If the REE-rich apatite had formed later, for instance during a final stage of M1 monazite growth, then the La/Nd ratio should have been just elevated in the rim zones of M1 monazite and should have been close to the whole-rock values in the cores. However, this is not observed in the Pohorje gneiss. Therefore, we suggest that M1 monazite formed synchronously with an REE-rich apatite in this rock, in conjunction with allanite breakdown at elevated pressures. It is important to note that all apatite inclusions shielded by garnet, which should be relics of the prograde medium-pressure stage according to the garnet-growth isopleths in Figure 9, have a low REE content (Table 3) and that secondary monazite inclusions are only rarely seen within them. These relict medium-pressure apatite grains are therefore likely to never have been as REE-rich as the apatite grains that equilibrated with M1 monazite during the high-*P* stage. This is another indication that REE partitioning into the apatite took place during the high-*P* stage.

Finger and Krenn (2007) have recently documented a high-pressure/high-temperature rock, in which a first monazite generation that formed from prograde breakdown of allanite underwent a strong dissolution at the *P-T* peak (2.8 GPa, 830 °C). At the same time, a REE-rich, high-*P* apatite formed (being preserved as inclusions in garnet in this case!) and a new Th-rich, peak *P-T* monazite reprecipitated around the older monazite. This led to very complex monazite zoning patterns. Such dissolution-reprecipitation patterns are not seen in M1 monazites of the Pohorje gneiss. This absence may indicate that M1 monazite in this rock formed close to the *P-T* peak and directly from the allanite, whereas in the case of the high-*P*/high-*T* rock reported by Finger and Krenn (2007) another earlier (medium-pressure?) monazite generation was apparently involved, which may have formed from the allanite as well, but not in paragenesis with a REE-rich apatite. This scenario could occur, for example, along the prograde path I shown in Figure 9. Medium-pressure monazite that formed in the Bt-Phg-St-Grt-Qtz and the Bt-Phg-Grt-Ky-Qtz fields, may become unstable during further pressure increase as a consequence of the increased REE uptake capacity of apatite at high-*P* conditions.

LREE-partitioning between monazite and apatite

A necessary conclusion from the foregoing discussion is that the apatite in the rock was REE-enriched during the high-*P* stage. Two different approaches can be invoked in an effort to estimate the former LREE content of the high-*P* apatite. (1) The volume ratio of M1:M2 monazite in thin section is approximately 70:30. Assuming that the M2 monazite has obtained its REEs solely from the high-*P* apatite, then the latter should have contained roughly 30% of the LREE whole-rock budget (i.e., ~40 ppm LREE; see Table 2). This would equal an average LREE concentration of ca. 1 wt% in the high-*P* apatite, according to the modal proportion of ca. 0.4 wt% apatite (Table 2). There are two uncertainties involved in this estimation. First, M2 monazite (in particular the M2-c and M2-d subtypes) may also contain LREEs from an M1 monazite source. Second, relict apatite shielded in the garnet could not take up LREEs during the high-*P* stage.

Since these effects counter each other, the above estimate of 1 wt% may still be reasonably correct. It would thus appear that the LREE content of the high-*P* apatite was just moderately high, but by no means extremely high. And (2), the density of M2-a monazite needles within apatite was never observed to be greater than a volume ratio of 1 mnz:30 ap. This would further suggest that the LREE content of the high-*P* apatite was not higher than 1–2 wt%.

Assuming (based upon the mean M2 composition) that the high-*P* apatite had an average LREE content of 1 wt% at a La content of ~0.2 wt% and Nd content of ~0.4 wt%, values of a distribution coefficient, $D^{La}_{Mnz/Ap}$, of ~70 and ~30 for $D^{Nd}_{Mnz}Ap$ can be estimated for the high-*P* stage using the mean M1 monazite composition. Likewise, a somewhat lower $D^{Sm}_{Mnz/Ap}$ value of ~20 can be inferred for this stage.

As shown by the microprobe data for matrix apatite and M2 monazite, the distribution coefficients $D^{La}_{Mnz/Ap}$ and $D^{Nd}_{Mnz/Ap}$ definitely exceed 100 for the retrograde stage. This reinforces earlier ideas (Spear and Pyle 2002; Finger and Krenn 2007) that the LREEs tend to partition from monazite into apatite at high-*P* conditions and from apatite into monazite at low-*P* conditions. The LREE transfer between the two minerals will be most effective when temperatures are high enough to warrant rapid REE equilibration within the apatite structure. Since M2-a monazite inclusions are also found within the core zones of larger apatite (Fig. 4b), we conclude that diffusion was fast enough to allow a complete reequilibration of the pre-existing apatite with REEs during the high-*P* stage.

Acknowledgments

This work was supported by the Austrian Science Foundation (FWF, grant P18070 to F.F), by the Slovak Research and Development Agency, project APVV-51-046105 and the VEGA Scientific Grant Agency (grant No. 2/6092/26). This paper was greatly improved following thorough reviews of Peter S. Dahl and Callum J. Hetherington. Peter Dahl is also thanked for the editorial handling.

References cited

Ayers, J.C., Miller, C., Gorisch, B., and Milleman, J. (1999) Textural development of monazite during high-grade metamorphism: Hydrothermal growth kinetics, with implications for U-Th-Pb geochronology. American Mineralogist, 84, 1766–1780.

Altherr, R., Lugovic, B., Meyer, H.P., and Majer, V. (1995) Early Miocene post-collisional calc-alkaline magmatism along the easternmost segment of the periadriatic fault system (Slovenia and Croatia). Mineralogy and Petrology, 54, 225–247.

Berman, R.G. (1990) Mixing properties of Ca-Mg-Fe-Mn garnets. American Mineralogist, 75, 328–344.

Bingen, B., Demaiffe, D., and Hertogen, J. (1996) Redistribution of rare earth elements, thorium, and uranium over accessory minerals in the course of amphibolite to granulite facies metamorphism; the role of apatite and monazite in orthogneisses from south western Norway. Geochimica et Cosmochimica Acta, 60, 1341–1354.

Cho, M., Kim, Y., and Yi, K. (2006) Parageneses of allanite, monazite and xenotime in the Barrovian-type metapelites of the Imjingang belt, Central Korea: Implications for radioactive element partitioning. Geochimica et Cosmochimica Acta, 70, A101.

Cherniak, D.J. and Ryerson, F.J. (1993) A study of strontium diffusion in apatite using Rutherford backscattering spectroscopy and ion implantation. Geochimica et Cosmochimica Acta, 57, 4653–4662.

Cherniak, D.J., Watson, E.B., Grove, M., and Harrison, T.M. (2004) Pb diffusion in monazite: A combined RBS/SIMS study. Geochimica et Cosmochimica Acta, 68, 829–840.

Chopin, C. and Ferraris, G. (2003) Mineral chemistry and mineral reactions in UHPM rocks. In D.A. Carswell and R. Compagnoni, Eds., Ultrahigh-Pressure Metamorphism, 5, p. 191–227. European Notes in Mineralogy, Eötvös University Press, Budapest.

Connolly, J.A.D. (2005) Computation of phase-equilibria by linear programming: A tool for geodynamic modeling and its application to subduction zone decarbonation. Earth and Planetary Science Letters, 236, 524–541.

Cornell, D., Janák, M., Froitzheim, N., Broska, I., Vrabec, M., and de Hoog, C.J. (2007) Ion microprobe U-Pb zircon dating of gneiss from the Pohorje, Eastern Alps and implications for deep subduction of a coherent continental crust. 8th Workshop on Alpine Geological Studies, Davos, Switzerland, Abstract Volume, p. 15–16.

Corrie, S.L. and Kohn, M.J. (2008) Trace-element distributions in silicates during prograde metamorphic reactions: Implications for monazite formation. Journal of Metamorphic Geology, 26, 451–464.

Ferry, J.M. and Spear, F.S. (1978) Experimental calibration of the partitioning of Fe and Mg between biotite and garnet. Contributions to Mineralogy and Petrology, 66, 113–117.

Finger, F. and Krenn, E. (2007) Three metamorphic monazite generations in a high-pressure rock from the Bohemian Massif and the potentially important role of apatite in stimulating polyphase monazite growth along a *P-T* loop. Lithos, 95, 115–125.

Finger, F., Broska, I., Roberts, M.P., and Schermaier, A. (1998) Replacement of primary monazite by apatite-allanite-epidote coronas in an amphibolite facies granite gneiss from the eastern Alps. American Mineralogist, 83, 248–258.

Fleet, M.E. and Pan, Y. (1997) Rare earth elements in apatite: Uptake from H_2O-bearing phosphate-fluoride melts and the role of volatile components. Geochimica et Cosmochimica Acta, 61, 4745–4760.

Fodor, L., Balogh, K., and Dunkl, I. (2003) Structural evolution and exhumation of the Pohorje-Kozjak Mts., Slovenia. Annales Universitatis Scientarum Budapestinensis, Sectio Geologica, 35, 118–119.

Fodor, L., Gerdes, A., Dunkl, I., Koroknai, B., Pécskay, Z., Trajanova, M., Horváth, P., Vrabec, M., Jelen, B., Balogh, K., and Frisch, W. (2008) Miocene emplacement and rapid cooling of the Pohorje pluton at the Alpine-Pannonian-Dinaridic junction, Slovenia. Swiss Journal of Geosciences, 101, 255–271, DOI: 10.1007/s00015-008-1286-9.

Foster, G., Kinny, P., Vance, D., Prince, C., and Harris, N. (2000) The significance of monazite U-Th-Pb age data in metamorphic assemblages; a combined study of monazite and garnet chronometry. Earth and Planetary Science Letters, 181, 327–340.

Foster, G., Gibson, H.D., Parrish, R., Horstwood, M., Fraser, J., and Tindle, A. (2002) Textural, chemical and isotopic insights into the nature and behavior of metamorphic monazite. Chemical Geology, 191, 183–207.

Froitzheim, N., Schmid, S., and Frey, M. (1996) Mesozoic palaeography and the timing of eclogite-facies metamorphism in the Alps: a working hypothesis. Eclogae Geologicae Helvetiae, 89, 81–110.

Gibson, H.D., Carr, S.D., Brown, R.L., and Hamilton, M.A. (2004) Correlations between chemical and age domains in monazite, and metamorphic reactions involving major pelitic phases: an integration of ID-TIMS and SHRIMP geochronology with Y-Th-U X-ray mapping. Chemical Geology, 211, 237–260.

Gratz, R. and Heinrich, W. (1997) Monazite-xenotime thermobarometry: Experimental calibration of the miscibility gap in the binary system $CePO_4$-YPO_4. American Mineralogist, 82, 772–780.

Hansen, E. and Harlov, D.E. (2006) Fluorapatite and biotite chemistry in orthopyroxene-bearing migmatites: Examples from California and southern India. Geological Society of America. Abstracts with Programs, 38, 561.

——— (2007) Whole-rock, phosphate, and silicate compositional trends across an amphibolite- to granulite-facies transition, Tamil Nadu, India. Journal of Petrology, 48, 1641–1680.

Harlov, D.E. and Förster, H.J. (2002) High-grade fluid-metasomatism on both a local and regional scale: the seaward Peninsula, Alaska, and the Val Strona di Omega, Ivrea-Verbano Zone, Northern Italy. Part II: Phosphate mineral chemistry. Journal of Petrology, 43, 769–799.

Harlov, D.E., Wirth, R., and Förster, H.J. (2005) An experimental study of dissolution-reprecipitation in fluorapatite: Fluid infiltration and the formation of monazite. Contributions to Mineralogy and Petrology, 150, 268–286.

Heinrich, W., Andrehs, G., and Franz, G. (1997) Monazite-xenotim miscibility gap thermometry. I. An empirical calibration. Journal of Metamorphic Geology, 15, 3–16.

Hoinkes, G., Koller, F., and Ranitsch, G. (1999) Alpine metamorphism of the Eastern Alps. Schweizerische Mineralogische und Petrographische Mitteilungen, 79, 155–181.

Holland, T.J.B. and Powell, R. (1998) An internally consistent thermodynamic data set for phases of petrological interest. Journal of Metamorphic Geology, 16, 309–343.

Hurai, V., Janák, M., and Thomas, R. (2008) Fluid-induced metasomatism of garnet porphyroblasts from eclogite-hosted metapelites of Pohorje Mts., Slovenia. Proceedings from Workshop: Mineral Equilibria, Metasomatism, and Mass Transport: Evolution and Stabilisation of Rock on a Fluid-Rich World, Smolenice, Slovak Republic, April 8–10, 2008, p 58–63.

Hwang, S.L, Yui, T.F., Chu, H.T., Shen, P., Schertl, H.P., Zhang, R.Y., and Liou, J.G. (2007) On the origin of oriented rutile needles in garnet from UHP eclogites. Journal of Metamorphic Geology, 25, 349–362.

Janák, M., Froitzheim, N., Lupták, B., Vrabec, M., and Krogh Ravna, E.J. (2004)

First evidence for ultrahigh-pressure metamorphism of eclogites in Pohorje, Slovenia: Tracing deep continental subduction in the Eastern Alps. Tectonics, 23, TC5014.

Janák, M., Froitzheim, N., Vrabec, M., Krogh Ravna, E.J., and De Hoog, J.C.M. (2006) Ultrahigh-pressure metamorphism and exhumation of garnetperidotite in Pohorje, Eastern Alps. Journal of Metamorphic Geology, 24, 19–31.

Janots, E., Negro, F., Brunet, F., Goffe, B., Engi, M., and Bouybaouene, M.L. (2006) Evolution of the REE mineralogy in HP-LT metapelites of the Sebtide complex, Rif, Marocco: Monazite stability and geochronology. Lithos, 87, 214–234.

Janots, E., Brunet, F., Goffe, B., Poinssot, C., Burchard, M., and Cemic, L. (2007) Thermochemistry of monazite-(La) and dissakisite (La): Implications for monazite and allanite stability inmetapelites. Contributions to Mineralogy and Petrology, 154, 1–14.

Janots, E., Engi, M., Berger, A., Allaz, J., Schwarzc J.-O., and Spandler, C. (2008) Prograde metamorphic sequence of REE minerals in pelitic rocks of the Central Alps: implications for allanite-monazite-xenotime phase relations from 250 to 610 °C. Journal of Metamorphic Geology, 26, 509–526.

Jeřábek, P., Janák, M., Faryad, S.W., Finger, F., and Konečný, P. (2008) Polymetamorphic evolution of pelitic schists and evidence for Permian low-pressure metamorphism in the Vepor Unit, West Carpathians. Journal of Metamorphic Geology, 26, 465–485.

Jercinovic, M.J. and Williams, M.L. (2005) Analytical perils (and progress) in electron microprobe trace element analysis applied to geochronology: background acquisition, interferences, and beam irradiation effects. American Mineralogist, 90, 526–546.

Kai, Y., Bolin, C., and Dania, Y. (2000) The possible subduction of continental material to depths greater than 200 km. Centre National de la Recherché Scientifique, 407, 734–736.

Kingsbury, J.A., Miller, C.F., Wooden, J.L., and Harrison, T.M. (1993) Monazite paragenesis and U-Pb systematics in rocks of the eastern Mojave Desert, California, U.S.A.; implications for thermochronometry. Chemical Geology, 110, 147–167.

Kohn, M.J. and Malloy, M.A. (2004) Formation of monazite via prograde metamorphic reactions among common silicates: Implications for age determinations. Geochimica et Cosmochimica Acta, 68, 101–113.

Konečný, P., Siman, P., Holický, I., Janák, M., and Kollárová, V. (2004) Method of monazite dating by means of the microprobe. Mineralia Slovaca, 36, 225–235.

Koziol, A.M. and Newton, R.C. (1988) Redetermination of the anorthite breakdown reaction and improvement of the plagioclase-garnet-Al_2SiO_5-quartz barometer. American Mineralogist, 73, 216–223.

Krenn, E. and Finger, F. (2004) Metamorphic formation of Sr-apatite and Sr-bearing monazite in a high pressure rock from the Bohemian Massif. American Mineralogist, 89, 1323–1329.

——— (2007) Formation of monazite and rhabdophane at the expense of allanite during Alpine low temperature retrogression of metapelitic basement rocks from Crete, Greece: Microprobe data and geochronological implications. Lithos, 95, 130–147.

Krenn, E., Ustaszewski, K., and Finger, F. (2008) Detrital and newly formed metamorphic monazite in amphibolite-facies metapelites from the Motajica Massif, Bosnia. Chemical Geology, 254, 164–174.

Kretz, R. (1983) Symbols for rock-forming minerals. American Mineralogist, 68, 277– 279.

Krogh Ravna, E.J. and Terry, M.P. (2004) Geothermobarometry of UHP and HP eclogites and schists—an evaluation of equilibria among garnet–clinopyroxene–kyanite–phengite–coesite/quartz. Journal of Metamorphic Geology, 22, 579–592.

Liou, J.G., Zhang, R.V., Ernst, W.G., Rumble, D.I., and Maruyama, S. (1998) High-pressure minerals from deeply subducted metamorphic rocks. In R.J. Hemley, Ed., Ultrahigh-Pressure Mineralogy: Physics and Chemistry of the Earth's Deep Interior, 37, p. 33–96. Reviews in Mineralogy, Mineralogical Society of America, Chantilly, Virginia.

Ludwig, K.R. (2001) Isoplot/Ex, Version 2.49e. A Geochronological Toolkit for Microsoft Excel. Berkeley Geochronological Center Special Publications, 1a.

Matsukage, K.N., Ono, S., Kawamoto, T., and Kikegawa, T. (2004) The compressibility of a natural apatite. Physics and Chemistry of Minerals, 31, 580–584.

McFarlane, C.R.M., Connelly, J.N., and Carlson, W.D. (2006) Contrasting response of monazite and zircon to a high-*T* thermal overprint. Lithos, 88, 135–149.

Miller, C., Mundil, R., Thöni, M., and Konzett, J. (2005) Refining the timing of eclogite metamorphism: a geochemical, petrological, Sm-Nd and U-Pb case study from the Pohorje Mountains, Slovenia (Eastern Alps). Contributions to Mineralogy and Petrology, 150, 70–84.

Mioč, P. and Žnidarčič, M. (1977) Geological map of SFRJ 1:100 000, Sheet Slovenj Gradec. Geological Survey, Ljubljana, Federal Geological Survey, Beograd.

Montel, J.M., Foret, S., Veschambre, M., Nicollet, C., and Provost, A. (1996) A fast, reliable, inexpensive in situ dating technique: Electron microprobe ages on monazite. Chemical Geology, 131, 37–53.

Mposkos, E.D. and Kostopoulos, D.K. (2001) Diamond, former coesite and supersilicic garnet in metasedimentary rocks from the Greek Rhodope: A new ultrahigh-pressure metamorphic province established. Earth and Planetary Science Letters, 192, 497–506.

Murayama, J.K., Makai, S., Kato, M., and Kumazawa, M. (1986) A dense polymorph of $Ca_3(PO_4)_2$: A high-pressure phase of apatite decomposition and its geochemical significance. Physics of the Earth and Planetary Interiors, 44, 293–303.

Nagy, G., Draganits, E., Demény, A., Pantó, G., and Arkai, P. (2002) Genesis and transformation of monazite, florencite, and rhabdophane during medium grade metamorphism: examples from the Sopron Hills, Eastern Alps. Chemical Geology, 191, 23–44.

Oberhänsli, R., Bousquet, R., and Engi, M. (2004) Metamorphic structure of the Alps. Metamorphic structure of the Alps. Scale 1:1.000.000. Mitteilungen der Österreichischen Mineralogischen Gesellschaft, 149, 277 (Kartenbeilage)

Neubauer, F. and Höck, V. (2000) Aspects of geology in Austria and adjoining areas: Introduction. Mitteilungen der Osterreichischen Mineralogischen Gesellschaft, 92, 7–14.

Newton, R.C., Charlu, T.V., and Kleppa, O.J. (1980) Thermochemistry of high structural state plagioclases. Geochimica et Cosmochimica Acta, 44, 933–941.

Pan, Y., Fleet, M.E., and Macrae, N.D. (1993) Oriented monazite inclusions in apatite porphyroblasts from the Hemlo gold deposit, Ontario, Canada. Mineralogical Magazine, 57, 697–707.

Pyle, J.M. and Spear, F.S. (1999) Yttrium zoning in garnet: coupling of major and accessory phases during metamorphic reactions. Geological Materials Research, 1, 1 –49.

——— (2003). Four generations of accessory phasegrowth in low-pressure migmatites from SW New Hampshire, U.S.A. American Mineralogist, 88, 338–351.

Pyle, J.M., Spear, F.S., Rudnick, R.L., and McDonough, W.F. (2001) Monazite–xenotime–garnet equilibrium in metapelites and a new monazite–garnet thermometer. Journal of Petrology, 42, 2083–2107.

Rasmussen, B., Janet, R., and Muhling, J.R. (2007) Monazite begets monazite: Evidence for dissolution of detrital monazite and reprecipitation of syntectonic monazite during low-grade regional metamorphism. Contributions to Mineralogy and Petrology, 154, 675–689.

Ringwood, A.E. and Lovering, J.F. (1970) Significance of pyroxene-ilmenite intergrowths among kimberlite xenoliths. Earth and Planetary Science Letters, 7, 371–375.

Sassi, R., Mazzolli, C., Miller, C., and Konzett, J. (2004) Geochemistry and metamorphic evolution of the Pohorje Mountain eclogites from the easternmost Austroalpine basement of the Eastern Alps (Northern Slovenia). Lithos, 78, 235–261.

Sawka, W.N., Banfield, J.F., and Chappell, B.W. (1986) A weathering-related origin of widespread monazite in S-type granites. Geochimica et Cosmochimica Acta, 50, 171–175.

Scherrer, N.C., Gnos, E., and Chopin, C. (2001) A retrograde monazite-forming reaction in bearthite-bearing high-pressure rocks. Schweizerische Mineralogische und Petrographische Mitteilungen, 81, 369–378.

Schmid, S.M., Fügenschuh, B., Kissling, E., and Schuster, R. (2004) Tectonic map and overall architecture of the Alpineorogen. Eclogae Geologicae Helvetiae, 97, 93–117.

Schuster, R., Koller, F., Hoeck, V., Hoinkes, G., and Bousquet, R. (2004) Explanatory notes to the map: Metamorphic structure of the Alps, Metamorphic evolution of the Eastern Alps. Mitteilungen der Österreichischen Mineralogischen Gesellschaft, 149, 175–199.

Seydoux-Guillaume, A.-M., Wirth, R., Heinrich, W., and Montel, J.M. (2002) Experimental determination of thorium partitioning between monazite and xenotime using analytical electron microscopy and X-ray diffraction Rietveld analysis. European Journal of Mineralogy, 14, 869–878.

Spear, F.S. and Pyle, J.M. (2002) Apatite, monazite, and xenotime in metamorphic rocks. In M.L. Kohn, J. Rakovan, and J.M. Hughes, Eds., Phosphates—Geochemical, Geobiological, and Materials Importance, 48, p. 293–335. Reviews in Mineralogy and Geochemistry, Mineralogical Society of America, Chantilly, Virginia.

Stampfli, G.M., Mosar, J., Marquer, D., Marchant, R., Baudin, T., and Borel, G. (1998) Subduction and obduction processes in the Swiss Alps. Tectonophysics, 296, 159–204.

Suzuki, K., Adachi, M., and Tanaka, T. (1991) Middle Precambrian provenance of Jurassic sandstone in the Mino Terrane, central Japan: Th-U-total Pb evidence from an electron microprobe monazite study. Sedimentary Geology, 75, 141–147.

Tacker, R.C. and Stormer, J.C. (1989) A thermodynamic model for apatite solid solutions applicable to high-temperture geological problems. American Mineralogist, 74, 877–888.

Thöni, M. (2002) Sm-Nd isotope systematics in garnet from different lithologies (Eastern Alps): Age results, and an evaluation of potential problems for garnet Sm-Nd chronometry. Chemical Geology, 185, 255–281.

Thöni, M. and Jagoutz, E. (1992) Some new aspects of dating eclogites in orogenic belts: Sm-Nd, Rb-Sr, and Pb-Pb isotopic results from the Austroalpine Saualpe and Koralpe typelocality (Carinthia/Styria, southeastern Austria). Geochimica

et Cosmochimica Acta, 56, 347–368.
Thompson, R.N. (1975) Is upper-mantle phosphorous contained in sodic garnet? Earth and Planetary Science Letters, 2, 417–424.
Tomkins, H.S. and Pattison, D.R.M. (2007) Accessory phase petrogenesis in relation to major phase assemblages in pelites from the Nelson contact aureole, southern British Columbia. Journal of Metamorphic Geology, 25, 401–421.
Trajanova, M., Pécskay, Z., and Itaya, T. (2008) K-Ar geochronology and petrography of the Miocene Pohorje Mountains batholith (Slovenia). Geologica Carpathica, 59, 247–260.
Watson, E. and Green, T.H. (1981) Apatite/liquid partition coefficients for the rare earth elements and strontium. Earth and Planetary Science Letters, 56, 405–421.
Wing, B., Ferry, J.M., and Harrison, T.M. (2003) Prograde destruction and formation of monazite and allanite during contact and regional metamorphism of pelites: Petrology and geochronology. Contributions to Mineralogy and Petrology, 145, 228–250.
Yang, P.S. and Pattison, D.R.M. (2006). Genesis of monazite and Y zoning in garnet from the Black Hills, South Dakota. Lithos, 88, 233–253.
York, D. (1966) Least-squares fitting of a straight line. Canadian Journal of Physics, 44, 1079–1086.
Zhang, R.Y. and Liou, J.G. (1999) Exsolution lamellae in minerals from ultrahigh-pressure rocks. International Geology Review, 41, 981–993.
——— (2003) Clinopyroxenite from the Sulu ultrahigh-pressure terrane, eastern China: Origin and evolution of garnet exsolution in clinopyroxene. American Mineralogist, 88, 1591–1600.
Zhu, X.K. and O'Nions, R.K. (1999a) Zonation of monazite in meatmorphic rocks and its implications for high temperature thermochronology: A case study from the Lewisian Terrain. Earth and Planetary Science Letters, 171, 209–220.
——— (1999b) Monazite chemical composition: Some implications for monazite geochronology. Contributions to Mineralogy and Petrology, 137, 351–363.
Ziemann, M.A., Forster, H.J., Harlov, D.E., and Frei, D. (2005) Origin of fluor-apatite-monazite assemblages in a metamorphosed, sillimanite-bearing pegmatoid, Reinbolt Hills, East Antarctica. European Journal of Mineralogy, 17, 567–579.

Manuscript received March 21, 2008
Manuscript accepted January 16, 2009
Manuscript handled by Peter Dahl